Impact of Surface Adsorbates and Dimensionality on Templating of Halide Perovskites

Erik Fransson, Julia Wiktor, and Paul Erhart
*Department of Physics, Chalmers University of Technology, SE-41296, Gothenburg, Sweden**

Two-dimensional (2D) halide perovskites (HPs) are promising materials for various optoelectronic applications, yet a comprehensive understanding of their dynamics is still elusive. Here, we offer insight into the dynamics of prototypical 2D HPs based on $MAPbI_3$ as a function of linker molecule and the number of perovskite layers using atomic scale simulations. We show that the layers closest to the linker undergo transitions that are distinct from those of the interior layers. These transitions can take place anywhere between a few tens of K below to more than 100 K above the cubic-tetragonal transition of bulk $MAPbI_3$. In combination with the thickness of the perovskite layer this enables one to template phase transitions and tune the dynamics over a wide temperature range. Our results thereby reveal the details of an important and generalizable design mechanism for tuning the properties of these materials.

Halide perovskites (HPs) are a promising class of materials for various applications, including, e.g., high-efficiency solar cells, [1–3] lasers [4] and light emitting diodes [5]. The most studied so far are the regular three-dimensional HPs with the formula AMX_3, where A is an organic or inorganic cation, M is a metal cation, such as Pb or Sn, and X is a halogen. One of the drawbacks of these compounds is that they often exhibit relatively low stability. In recent years, so-called two-dimensional (2D) HPs (also referred to as layered, quasi-2D or Ruddlesden-Popper phases) [6] have, however, gained significant attention [7–10]. These materials are composed of inorganic perovskite layers stacked on top of each other and separated by organic cations that act as spacers (Fig. 1) [11–16]. They have been shown to exhibit improved stability [17–25] and distinct quantum and dielectric confinement effects [26–28], which modulate their excitonic properties [29–31], differentiating them from their 3D counterparts. In combination with their tunability [32, 33], this makes 2D HPs highly attractive for various optoelectronic applications [18, 33–37].

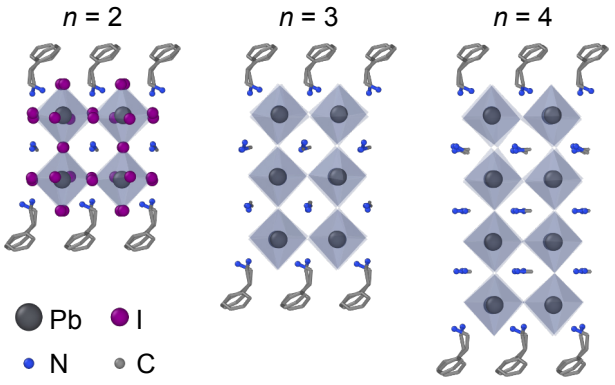

FIG. 1. PEA-based 2D HP phases with the composition $PEA_2MA_{n-1}Pb_nI_{3n+1}$ for $n = 2$, 3 and 4 layers. For $n > 2$ hydrogen and iodine atoms are omitted for clarity. The structures were rendered using OVITO [38].

* erhart@chalmers.se

The properties of 2D HPs sensitively depend on the number and type of inorganic layers and the organic cations that connect them [10, 13, 39–41]. The inorganic layers are responsible for the electronic structure [42–44] and mechanical properties of the material, while the organic cations affect the interlayer spacing as well as the overall stability and structure. Therefore, understanding the interplay of inorganic layers and organic cations is crucial for designing efficient and stable optoelectronic devices based on these materials. This is evident in the so-called "templating" approach [45–49]. This strategy relies on the fact that the organic linkers can significantly affect the phase of the inorganic framework beyond the surface layer, which can be used to improve the stability of the desired 3D perovskite phases. To be able to fully exploit the potential of this approach, it is, however, necessary to understand the precise mechanisms by which organic cations influence the inorganic framework.

Here, we offer comprehensive insight into how phase transitions and dynamics in 2D HPs can be steered through the choice of the organic linker molecule and the dimensionality of the material. This is accomplished through atomic scale simulations based on accurate and efficient machine learning potentials (MLPs) trained against density functional theory (DFT) calculations. We first focus on the prototypical combination of the linker molecule phenylethylammonium $C_6H_5(CH_2)_2NH_3$ (PEA) with $MAPbI_3$ and identify a transition from a high-temperature structure without global octahedral tilting to a lower temperature structure with a global out-of-phase octahedral tilting pattern. The perovskite layer in direct contact with the PEA molecules (referred to as "surface layer" below) undergoes a transition already between 450 and 470 K, while the transition in the interior of the perovskite slab occurs at a temperature that is at least 50 K lower. The combination of these two processes yields a rather broad overall transition, which approaches the transition temperature of bulk $MAPbI_3$ only for relatively thick inorganic layers comprising at least 30 or more perovskite layers. To generalize the effect of the linker molecule on the local phase transitions, we then extend the analysis to additional molecules, including phenylmethylammonium $C_6H_5(CH_2)NH_3$ (PMA), buty-

lammonium $CH_3(CH_2)_3NH_3$ (BA) and methylammonium CH_3NH_3 (MA). We find that for bulkier molecules like PEA and PMA, the surface layer transitions significantly above the bulk $MAPbI_3$ transition, while with the smallest molecule, MA, this transition occurs at a lower temperature. Our results thereby provide an atomic scale understanding of how linker and dimensionality can be used to template phase behavior and dynamics in 2D HPs. Since octahedral tilting is intimately tied to the electronic structure [50–53], our results reveal the details of an important and generalizable design mechanism for tuning the optoelectronic properties of 2D HPs.

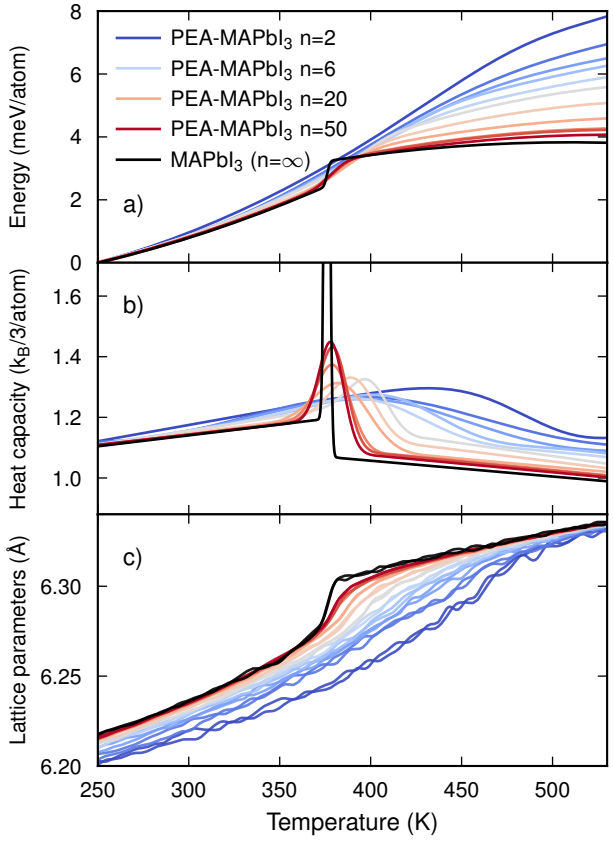

FIG. 2. Thermodynamic observables as a function of temperature from cooling simulations. (a) Potential energy (with $1.5k_BT$ and arbitrary reference energy subtracted) for the a series of 2D HPs with composition $PEA_2MA_{n-1}Pb_nI_{3n+1}$, which yields $MAPbI_3$ in the bulk limit ($n \to \infty$). (b) Heat capacity of the system obtained as $C_p = dE/dT$. (c) In-plane lattice parameters. For $MAPbI_3$ this corresponds to the a and b lattice parameters and the tilting in the $a^0a^0c^-$ phase occurs around the z-axis. The potential energy (and heat capacity) shown here are represented by fits to the raw data show in Fig. S2.

Thermodynamic properties. We consider a series of 2D HPs assembled from inorganic PbI_6 octahedral units with MA counterions and PEA linker molecules with the chemical formula $PEA_2MA_{n-1}Pb_nI_{3n+1}$, where n is the number of *perovskite* layers in each inorganic layer (Fig. 1). In the bulk limit ($n \to \infty$) one obtains $MAPbI_3$, which is one of the most widely investigated 3D HPs. We only consider systems with $n \geq 2$ since in the single perovskite layer limit ($n = 1$) we do not observe an untilted inorganic layer even at 600 K.

First, we analyze the potential energy, the heat capacity and the lattice parameters during cooling simulations (Fig. 2). The potential energy of $MAPbI_3$ shows a small but clear step at 370 K, corresponding to the latent heat associated with its first-order transition from a cubic $a^0a^0a^0$ phase to a tetragonal $a^0a^0c^-$ phase (Fig. 2a) [54]. This gives rise to a sharp peak in the heat capacity at the transition temperature (Fig. 2b). Additionally, the transition can be seen as a clear change in the two in-plane lattice parameters (tilting is around the out-of-plane axis; Fig. 2c) and even the out-of-plane lattice parameter (Fig. S4). The simulations yield a transition temperature for $MAPbI_3$ of 370 K, which is approximately 40 K higher than the experimental value of about 330 K [12, 55].

Comparable transitions are observed in the two-dimensional HPs. For smaller numbers of inorganic layers, n, the transition is more gradual and occurs at higher temperatures, but it becomes more pronounced as n increases, converging toward the behavior observed in $MAPbI_3$ as n increases. This shows that the nature of the phase transition evolves from a continuous to a first-order transition.

Octahedral tilting. To obtain a more detailed understanding of the transitions we compute the distribution over octahedral tilt angles $P(\theta)$ along the cooling simulations using OVITO [38] as done in Ref. 56 (Fig. 3). The tilt angle distribution for a given temperature is averaged over a few snapshots corresponding to a temperature window of about 1 K in order to improve the statistics.

For bulk $MAPbI_3$ one observes a sharp transition at 370 K from a single Gaussian peak centered around zero corresponding to a cubic phase ($a^0a^0a^0$) to a symmetric bimodal distribution indicating the transition to a structure with out-of-phase tilting ($a^0a^0c^-$; Fig. 3, bottom panel).

For the 2D HPs we can resolve the tilt angle distribution for each symmetrically distinct perovskite layer throughout the structure. This analysis reveals that the perovskite layer that is in direct contact with the PEA linker molecules (the "surface layers") undergoes a transition to a tilted structure that for, e.g., $n = 8$ occurs at around 450 K (Fig. 3; top panel). In contrast, the interior perovskite layers undergo a transition at a much lower temperature, i.e., closer to the bulk $MAPbI_3$ transition temperature, e.g., at around 400 K for $n = 8$, . It is worth noting that the transition in the surface layers has almost no impact on the tilting in the neighboring layer (layer 2 in Fig. 3; also compare Fig. 4b and Fig. 5b). We attribute this behavior to the octahedra rotating around the z-axis, leading to a weak correlation between neighboring octahedra in the z-direction [56, 57].

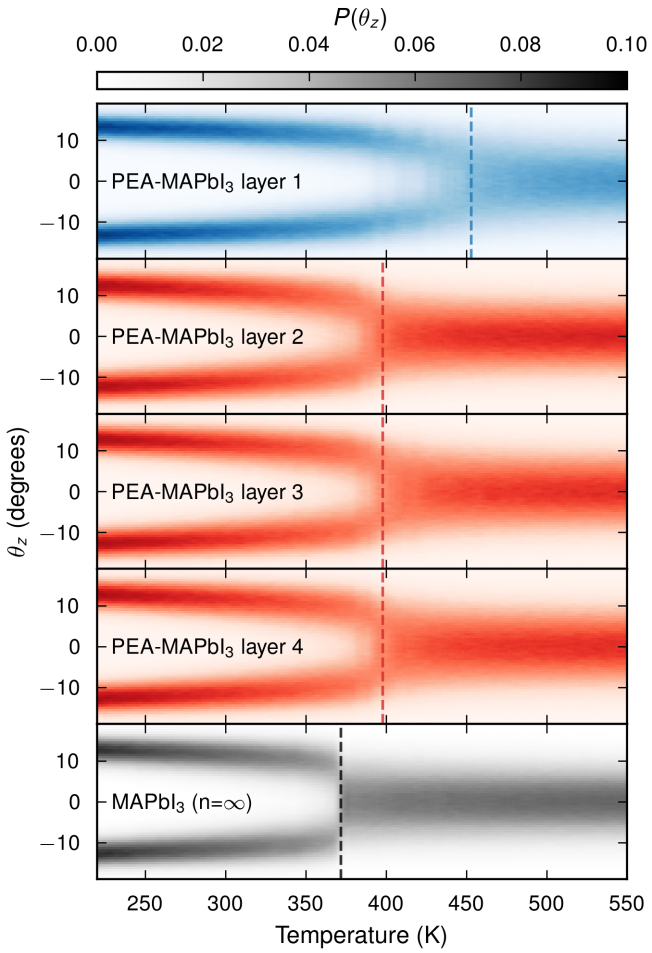

FIG. 3. Distribution over the octahedral tilt angles $P(\theta_z)$ as a function of temperatures for a 2D HP $PEA_2MA_{n-1}Pb_nI_{3n+1}$ with $n = 8$ as well as the corresponding 3D HP ($MAPbI_3$). For the 2D HP the tilt angle distribution is decomposed by perovskite layer, where layer 1 refers to the perovskite layer closest to the organic linker molecule.

At high temperatures, for which no global tilting pattern occurs, the tilt angle distributions are unimodal and well described by Gaussians with zero mean. The width of the distribution is, however, wider for the surface layers compared to the rest of the layers indicating a softer free energy landscape. Furthermore, at low temperature, for which all octahedra exhibit a tilt, the surface layers show slightly larger tilt (Fig. S5). Both of these observations are consistent with the surface layers exhibiting a higher transition temperature.

Phase diagram. The spatial variation of the evolution of octahedral tilts means that the PEA based 2D HPs internally undergo two transitions that can be observed separately in our simulations. The first one is associated with the tilting of the octahedra in the *surface* layer, while the second one is related to the tilting of the *interior* layers. Extending the tilt-angle analysis for n ranging from 2 to 50 allows us to obtain the variation of the two transition temperatures with n (Fig. 4). (For a brief discussion of the uncertainties in the transitions temperatures please see Sect. 3 in the Supplemental Material.) This shows that the transition in the surface layer depends only weakly on n varying from 470 K ($n = 2$) to about 450 K (large-n limit). The transition in the interior, which can only be identified for $n \geq 4$, exhibits a more pronounced dependence on n starting at about 410 K for $n = 4$ and converging to the bulk $MAPbI_3$ value of 370 K in the large-n limit.

The different structure of the surface layer compared to the interior resembles surface (interface) phases, also referred to as complexions [58, 59]. This type of surface phases can be understood from a simplified thermodynamic viewpoint using surface and interface free energies γ [60]. In this view, the above observation suggests that the effective interface free energy between the cubic phase and the organic linkers $\gamma_{\mathrm{cub/PEA}}$ is larger than the sum of the interface energy between the tetragonal phase and the organic linkers $\gamma_{\mathrm{cub/tet}}$, and the tetragonal and cubic phases $\gamma_{\mathrm{tet/PEA}}$, i.e., $\gamma_{\mathrm{cub/PEA}} > \gamma_{\mathrm{cub/tet}} + \gamma_{\mathrm{tet/PEA}}$.

In our simulations, the tilting of the two surface layers on the opposite sides of the inorganic slab are not correlated with each other at the upper transition temperature and can thus occur by chance in-phase or out-of-phase. For the out-of-phase tilting pattern ($a^0a^0c^-$) to be commensurate with both surface layers, the latter need to tilt out-of-phase or in-phase with respect to each other for an even and odd number of layers, n, respectively. As a result anti-phase boundaries can be expected to appear with 50% probability at nucleation time and are commonly observed in our simulations (Fig. 4). In some cases we observe such defects to anneal out already on the time scale of our simulations. Under experimental settings one can therefore assume that such defects typically anneal out and are only present in small concentrations.

Lastly, we look at the ordering of the linker molecules. The two layers of PEA forming a single organic spacer layer are always rotated 180° around the z-axis relative to each other (Fig. 1). In addition, we observe that the different spacer layers can take on arbitrary 90 and 180° rotations around the z-axis (see e.g., Fig. 4). This leads to the in-plane lattice parameters being equal (see Fig. 2). Reorientation and rotation of the spacer layers mainly take places during the equilibration part of the simulations, and appear to occur statistically. The orientation subsequently remains largely unaffected as temperature is reduced.

Extension to other systems. Now that we have seen how PEA templates the phase transition in the perovskite layers, it is instructive to extend the analysis to other linker molecules. To this end, we consider 2D HPs based on PMA and BA as well as MA-terminated surfaces, specifically {001} slabs of $MAPbI_3$ with MAI_2 termination (Fig. 5).

For **PMA** the behavior is qualitatively similar to that of PEA (Fig. S6), i.e., a transition of the octahedral tilt-

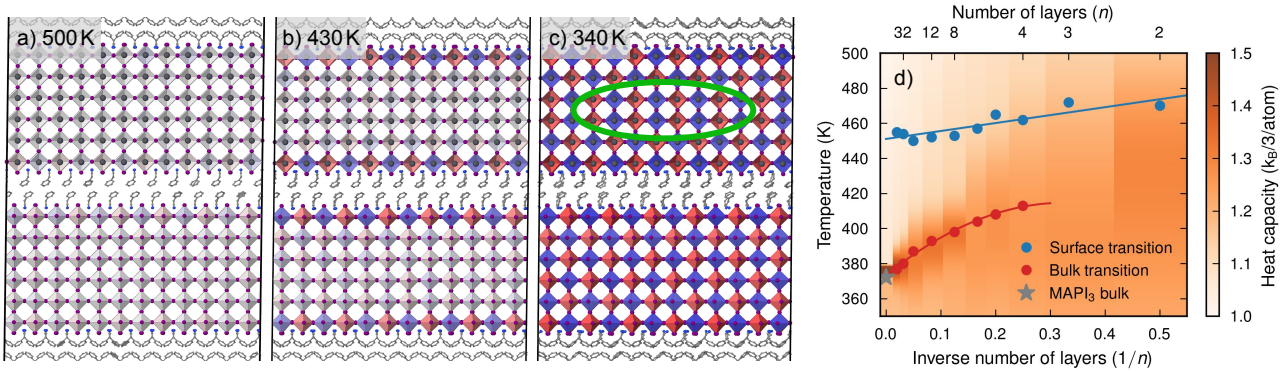

FIG. 4. Time-averaged snapshots from the cooling simulations for the 2D HP $PEA_2MA_{n-1}Pb_nI_{3n+1}$ with $n = 6$ at (a) 500 K, (b) 430 K and (c) 330 K visualized using OVITO [38]. Here, hydrogen atoms as well as the MA counterions inside the perovskite layers are omitted for clarity. The color coding of the octahedra indicates the rotation angle around the z-axis, θ_z, with red and blue indicating negative and positive tilting (ranging from -20 to 20°), respectively, while gray implies tilt angles close to zero. For 330 K a stacking fault (anti-phase boundary) is formed as highlighted by the green ellipsoid. (d) Transition temperatures as a function of number of layers n with the heat capacity (Fig. 2) shown as a heatmap.

ing pattern occurs in the surface layer at a temperature about 100 K higher than in the interior, albeit with a stronger dependence on the number of layers for the interior transition. Unlike the case of PEA for which we found tilting with respect to the out-of-plane axis (z), with PMA we obtain tilting around one of the in-plane axes (x or y).

For both PEA and PMA we observe that the transition temperature for the interior increases notably with decreasing number of layers, approaching the transition temperature for the surface for the thinnest slabs considered here. This reflects the increasing relative weight of the surface layer compared the rest of the system as n decreases. Similarly in the limit of large n, the interior transition temperature approaches that of bulk $MAPI_3$.

We also note that in the case of PMA we observe almost no anti-phase boundaries. We suggest this to be due to the stronger octahedral correlation *perpendicular* compared to *along* the rotational axis, as previously reported in bulk HPs [56, 57]. This likely leads to a stronger driving force for the (re)orientation of perovskite layers which is needed to avoid or anneal out anti-phase boundaries.

By contrast, in the case of **BA**, we observe no separation in temperature between the onset of tilting at the surface and the interior. Rather, there is just one transition that for the smallest n is barely 10 to 20 K higher than the phase transition temperature for bulk $MAPbI_3$ with a very weak dependence on the number of layers. Similarly to the case of PMA, for BA the tilting occurs around one of the in-plane axes. We note that one can observe a secondary transition associated with the motion and ordering of the BA linker molecules themselves (Fig. S9). At higher temperatures the BA molecules move much more freely than PEA and PMA [42], and are on average oriented perfectly perpendicular to the perovskite layers. Below 300 K this motion is, however, frozen out and the BA molecules become significantly stiffer.

For the **$MAPbI_3$ surface** we observe two different types of behavior. For thicker slabs ($n > 14$) the topmost (surface) layer undergoes a transition at a *lower* temperature than the interior region, thus exhibiting the opposite behavior compared to PEA and PMA. On the other hand, for thinner slabs ($n < 14$) the surface transition can no longer be separated from the transition in the interior of the slab. This can be at least partly explained by the transition temperature for the interior layers decreasing with the number of layers which causes the surface-to-interior ratio to increase. We also also observes a qualitative difference in the tilt pattern between thicker and thinner slabs as the former exhibit tilting with respect to the out-of-plane axis while for the latter tilting occurs with respect to one of the in-plane axes. This behavior suggests that the balance between surface and bulk energetics plays a key role here. While resolving the mechanism is beyond the scope of the present work it is deserving of a more in-depth analysis in future studies.

To summarize our analysis indicates that tilting behavior of the surface layer in 2D $MAPbI_3$-based perovskites, i.e., the softness of the rotational energy landscape of the octahedra, can be altered and controlled through the choice of the organic linker molecule. For the bulkier molecules, PEA and PMA, we find that the surface layer transitions at a considerably *higher* temperature than bulk $MAPbI_3$, whereas for the smallest molecule considered here, MA, we rather observe the surface transition to occur at a *lower* temperature than in the bulk. This leads to a transition temperature for the *interior* that decreases and increases with the number of layers for PEA/PMA and MA, respectively. For BA an intermediate behavior is observed, i.e., no separate transition for the surface layer. These results thus provide guiding principles for how both dimensionality (through the number of layers n) and chemistry (through the organic

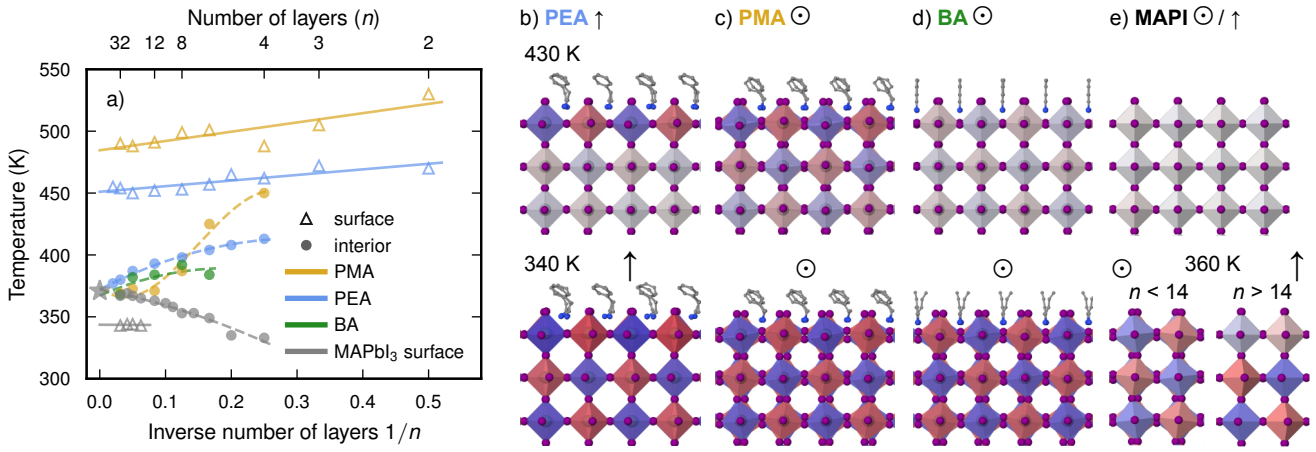

FIG. 5. (a) Transition temperatures as a function of the number of layers n for (b) PEA, (c) PMA and (d) BA-based 2D HPs as well as (e) $MAPbI_3$ surfaces. Triangles and circles indicate the transition temperatures for the surface layer and the interior layers, respectively. The star indicates the cubic-tetragonal phase transition temperature for bulk $MAPbI_3$. (b–e) Average atomic configurations at 430 K (top) and 340 K/360 K (bottom). Red and blue octahedra indicate negative and positive tilt angles (ranging from -20 to $20°$), respectively, whereas gray implies tilt angles close to zero. Arrows indicate the tilt axis, which is out-of-plane for PEA and $MAPbI_3$ surfaces with less than 14 layers, and in-plane for the other systems. Lines in (a) serve as a guide to the eye.

linkers) can be used to *systematically* tune the structural transitions and consequently the inorganic dynamics of the system. Both of these are directly tied to enhanced electron-phonon coupling, which is at the heart of the outstanding optoelectronic properties of these materials. The present insight is thereby of immediate interest for designing 2D HP materials and devices for specific applications and temperature ranges.

Acknowledgments. This work was supported by the Swedish Research Council (grant numbers 2020-04935, 2021-05072), the Chalmers Initiative for Advancement of Neutron and Synchrotron Techniques, the Swedish Strategic Research Foundation through a Future Research Leader programme (FFL21-0129) and the Wallenberg Academy Fellow program (J. W.). The computations were enabled by resources provided by the National Academic Infrastructure for Supercomputing in Sweden (NAISS) at C3SE, NSC, and PDC partially funded by the Swedish Research Council through grant agreements no. 2022-06725 and no. 2018-05973 as well as the Berzelius resource provided by the Knut and Alice Wallenberg Foundation at NSC.

We thank Göran Wahnström, Rasmus Lavén, Maths Karlsson, Prakriti Kayastha and Lucy Whalley for helpful discussions on 2D perovskites.

Computational Methods. The PEA-based 2D HPs have a composition of $PEA_2MA_{n-1}Pb_nI_{3n+1}$ where n corresponds to the number of perovskite layers. Starting from known prototypes for $n = 1$ [15, 48, 61, 62], we construct structures with $n > 1$ by inserting the required number of perovskite layers (Fig. 1). These structures are then equilibrated by molecular dynamics (MD) simulations at 600 K to remove structural bias before the cooling simulations. This approach is also employed for PMA and BA using the prototype structures from Refs. 48, 61, 63.

Energies, forces and virials were obtained for the training structures via DFT calculations as implemented in the Vienna ab-initio simulation package [64–66] using the projector augmented wave method [67, 68] with a plane wave energy cutoff of 520 eV and the SCAN+VV10 exchange-correlation functional [69]. The Brillouin zone was sampled with automatically generated $\boldsymbol{k}$-point grids with a maximum spacing of 0.25 $Å^{-1}$.

We constructed a neuroevolution potential (NEP) model using the iterative strategy outlined in Ref. 70 using the GPUMD software [71–73]. Training structures included MD structures at various temperatures up to 600 K for bulk $MAPbI_3$, 2D HP structures with varying number of perovskite layers and three different organic linkers, PEA, PMA and BA. Additionally, prototype (primitive) structures with varying volume were included as well as a few dimer configurations. The MD structures were generated via an active learning strategy using earlier NEP model generations and selected according to their uncertainty, which was estimated from the predictions of an ensemble of models. The final NEP was then trained using all available training data. In total the training set consists of 616 structures, corresponding to a total of 120 000 atoms. For the final model, the root mean squared errors obtained by cross validation using 10 folds are 10 meV $atom^{-1}$ for the energies, 150 meV $Å^{-1}$ for the forces and 90 meV $atom^{-1}$ for the virials (Fig. S1).

All MD simulations were carried out with GPUMD [73, 74] with a timestep of 0.5 fs. The cooling simulations were run in the NPT ensemble by first heating the system up

from zero to 600 K over 1 ns, followed by equilibration at 600 K for 1 ns, before finally cooling down to 200 K over 25 ns. Simulations were carried using cells comprising $6 \times 6 \times 4$ repetitions of the 2D prototype structures which for, e.g., $n = 12$ corresponds to about 50 000 atoms and a cell size of about 50 Å × 50 Å × 350 Å; see Fig. S3 for convergence testing.

The transitions between different perovskite phases were analyzed using the octahedral tilt angles of the PbI_6 octahedra [56, 57, 75, 76]. The tilt angles in the perovskite layers during MD simulations were obtained using OVITO [38] as implemented in Ref. 56.

Data availability. The DFT data and NEP model generated in this study are publicly available via Zenodo at `https://doi.org/10.5281/zenodo.11120638`.

[1] A. Kojima, K. Teshima, Y. Shirai, and T. Miyasaka, Journal of the American Chemical Society **131**, 6050 (2009).
[2] H.-S. Kim, C.-R. Lee, J.-H. Im, K.-B. Lee, T. Moehl, A. Marchioro, S.-J. Moon, R. Humphry-Baker, J.-H. Yum, J. E. Moser, M. Grätzel, and N.-G. Park, Scientific Reports **2**, 1 (2012).
[3] G. Hodes, Science **342**, 317 (2013).
[4] L. Lei, Q. Dong, K. Gundogdu, and F. So, Advanced Functional Materials **31**, 2010144 (2021).
[5] Q. Van Le, H. W. Jang, and S. Y. Kim, Small Methods **2**, 1700419 (2018).
[6] Q. A. Akkerman and L. Manna, ACS Energy Letters **5**, 604 (2020).
[7] C. C. Stoumpos, D. H. Cao, D. J. Clark, J. Young, J. M. Rondinelli, J. I. Jang, J. T. Hupp, and M. G. Kanatzidis, Chemistry of Materials **28**, 2852 (2016).
[8] D. H. Cao, C. C. Stoumpos, O. K. Farha, J. T. Hupp, and M. G. Kanatzidis, Journal of the American Chemical Society **137**, 7843 (2015).
[9] H. Tsai, W. Nie, J.-C. Blancon, C. C. Stoumpos, R. Asadpour, B. Harutyunyan, A. J. Neukirch, R. Verduzco, J. J. Crochet, S. Tretiak, L. Pedesseau, J. Even, M. A. Alam, G. Gupta, J. Lou, P. M. Ajayan, M. J. Bedzyk, M. G. Kanatzidis, and A. D. Mohite, Nature **536**, 312 (2016).
[10] G. Grancini and M. K. Nazeeruddin, Nature Reviews Materials **4**, 4 (2019).
[11] D. B. Mitzi, C. A. Feild, W. T. A. Harrison, and A. M. Guloy, Nature **369**, 467 (1994).
[12] C. C. Stoumpos, C. D. Malliakas, and M. G. Kanatzidis, Inorganic Chemistry **52**, 9019 (2013).
[13] L. Mao, C. C. Stoumpos, and M. G. Kanatzidis, Journal of the American Chemical Society **141**, 1171 (2018).
[14] Y. Han, S. Yue, and B.-B. Cui, Advanced Science **8**, 2004805 (2021).
[15] T. Liu, N. P. Holzapfel, and P. M. Woodward, IUCrJ **10**, 385 (2023).
[16] Akriti, J. Y. Park, S. Zhang, and L. Dou, Dimensionality modulation in halide perovskites, in *Halide Perovskite Semiconductors* (John Wiley & Sons, Ltd, 2024) Chap. 4, pp. 79–114.
[17] I. C. Smith, E. T. Hoke, D. SolisIbarra, M. D. McGehee, and H. I. Karunadasa, Angewandte Chemie International Edition **53**, 11232 (2014).
[18] L. Etgar, Energy and Environmental Science **11**, 234 (2018).
[19] H. Tsai, W. Nie, J.-C. Blancon, C. C. Stoumpos, C. M. M. Soe, J. Yoo, J. Crochet, S. Tretiak, J. Even, A. Sadhanala, G. Azzellino, R. Brenes, P. M. Ajayan, V. Bulovi, S. D. Stranks, R. H. Friend, M. G. Kanatzidis, and A. D. Mohite, Advanced Materials **30**, 1704217 (2018).
[20] C. Liu, W. Huhn, K.-Z. Du, A. Vazquez-Mayagoitia, D. Dirkes, W. You, Y. Kanai, D. B. Mitzi, and V. Blum, Physical Review Letters **121**, 146401 (2018).
[21] J. Leveillee, C. Katan, J. Even, D. Ghosh, W. Nie, A. D. Mohite, S. Tretiak, A. Schleife, and A. J. Neukirch, Nano Letters **19**, 8732 (2019).
[22] A. Mahata, D. Meggiolaro, L. Gregori, and F. De Angelis, The Journal of Physical Chemistry C **125**, 10901 (2021).
[23] E. Mosconi, A. A. Alothman, R. Long, W. Kaiser, and F. De Angelis, ACS Energy Letters **8**, 748 (2022).
[24] J. Y. Park, R. Song, J. Liang, L. Jin, K. Wang, S. Li, E. Shi, Y. Gao, M. Zeller, S. J. Teat, P. Guo, L. Huang, Y. S. Zhao, V. Blum, and L. Dou, Nature Chemistry **15**, 1745 (2023).
[25] C. T. Triggs, R. D. Ross, W. Mihalyi-Koch, C. F. M. Clewett, K. M. Sanders, I. A. Guzei, and S. Jin, ACS Energy Letters , 1835 (2024).
[26] J. Even, L. Pedesseau, and C. Katan, ChemPhysChem **15**, 3733 (2014).
[27] B. Traore, L. Pedesseau, L. Assam, X. Che, J.-C. Blancon, H. Tsai, W. Nie, C. C. Stoumpos, M. G. Kanatzidis, S. Tretiak, A. D. Mohite, J. Even, M. Kepenekian, and C. Katan, ACS Nano **12**, 3321 (2018).
[28] C. Katan, N. Mercier, and J. Even, Chemical Reviews **119**, 3140 (2019).
[29] M. Dyksik, H. Duim, D. K. Maude, M. Baranowski, M. A. Loi, and P. Plochocka, Science Advances **7**, eabk0904 (2021).
[30] Y. Shao, W. Gao, H. Yan, R. Li, I. Abdelwahab, X. Chi, L. Rogée, L. Zhuang, W. Fu, S. P. Lau, S. F. Yu, Y. Cai, K. P. Loh, and K. Leng, Nature Communications **13**, 10.1038/s41467-021-27747-x (2022).
[31] J. J. P. Thompson, M. Dyksik, P. Peksa, K. Posmyk, A. Joki, R. Perea-Causin, P. Erhart, M. Baranowski, M. A. Loi, P. Plochocka, and E. Malic, Advanced Energy Materials **n/a**, 2304343 (2024).
[32] A. Mahata, E. Mosconi, D. Meggiolaro, and F. De Angelis, Chemistry of Materials **32**, 105 (2019).
[33] W. Mihalyi-Koch, G. Folpini, C. R. Roy, W. Kaiser, C.-S. Wu, K. M. Sanders, I. A. Guzei, J. C. Wright, F. De Angelis, D. Cortecchia, A. Petrozza, and S. Jin, Journal of the American Chemical Society **145**, 28111 (2023).
[34] W. Fu, H. Liu, X. Shi, L. Zuo, X. Li, and A. K.-Y. Jen, Advanced Functional Materials **29**, 1900221 (2019).
[35] Y. Chen, Y. Sun, J. Peng, J. Tang, K. Zheng, and Z. Liang, Advanced Materials **30**, 1703487 (2018).
[36] L. Qian, Y. Sun, M. Sun, Z. Fang, L. Li, D. Xie, C. Li, and L. Ding, Journal of Materials Chemistry C **7**, 5353 (2019).
[37] S. Yuan, T. Fang, B. Han, Q. Shan, C. Wei, X. Zheng,

X. Li, B. Xu, and H. Zeng, Advanced Functional Materials **n/a**, 2316206 (2024).
[38] A. Stukowski, Modelling and Simulation in Materials Science and Engineering **18**, 015012 (2009).
[39] X. Li, J. M. Hoffman, and M. G. Kanatzidis, Chemical Reviews **121**, 2230 (2021).
[40] F. Jahanbakhshi, M. Mladenovi, M. Dankl, A. Boziki, P. Ahlawat, and U. Rothlisberger, Helvetica Chimica Acta **104**, e2000232 (2021).
[41] R. L. Kingsford, S. R. Jackson, L. C. Bloxham, and C. G. Bischak, Journal of the American Chemical Society **145**, 11773 (2023).
[42] R.-I. Biega, M. Bokdam, K. Herrmann, J. Mohanraj, D. Skrybeck, M. Thelakkat, M. Retsch, and L. Leppert, The Journal of Physical Chemistry C **127**, 9183 (2023).
[43] J. D. Ziegler, K.-Q. Lin, B. Meisinger, X. Zhu, M. Kober-Czerny, P. K. Nayak, C. Vona, T. Taniguchi, K. Watanabe, C. Draxl, H. J. Snaith, J. M. Lupton, D. A. Egger, and A. Chernikov, ACS Photonics **9**, 3609 (2022).
[44] S. Krach, N. Forero-Correa, R.-I. Biega, S. E. Reyes-Lillo, and L. Leppert, Journal of Physics: Condensed Matter **35**, 174001 (2023).
[45] D. B. Mitzi, Inorganic Chemistry **39**, 6107 (2000).
[46] D. B. Mitzi, Journal of the Chemical Society, Dalton Transactions , 1 (2001).
[47] Z. Xu and D. B. Mitzi, Chemistry of Materials **15**, 3632 (2003).
[48] K.-z. Du, Q. Tu, X. Zhang, Q. Han, J. Liu, S. Zauscher, and D. B. Mitzi, Inorganic Chemistry **56**, 9291 (2017).
[49] J. V. Mili, S. M. Zakeeruddin, and M. Grätzel, Accounts of Chemical Research **54**, 2729 (2021).
[50] M. R. Filip, G. E. Eperon, H. J. Snaith, and F. Giustino, Nature Communications **5**, 5757 (2014).
[51] J. Wiktor, U. Rothlisberger, and A. Pasquarello, The Journal of Physical Chemistry Letters **8**, 5507 (2017).
[52] X.-G. Zhao, G. M. Dalpian, Z. Wang, and A. Zunger, Physical Review B **101**, 155137 (2020).
[53] O. Cannelli, J. Wiktor, N. Colonna, L. Leroy, M. Puppin, C. Bacellar, I. Sadykov, F. Krieg, G. Smolentsev, M. V. Kovalenko, A. Pasquarello, M. Chergui, and G. F. Mancini, The Journal of Physical Chemistry Letters **13**, 3382 (2022).
[54] E. Fransson, J. M. Rahm, J. Wiktor, and P. Erhart, Chemistry of Materials **35**, 8229 (2023).
[55] P. S. Whitfield, N. Herron, W. E. Guise, K. Page, Y. Q. Cheng, I. Milas, and M. K. Crawford, Scientific Reports **6**, 1 (2016).
[56] J. Wiktor, E. Fransson, D. Kubicki, and P. Erhart, Chemistry of Materials **35**, 6737 (2023).
[57] W. J. Baldwin, X. Liang, J. Klarbring, M. Dubajic, D. Dell'Angelo, C. Sutton, C. Caddeo, S. D. Stranks, A. Mattoni, A. Walsh, and G. Csányi, Small , 2303565 (2023).
[58] P. R. Cantwell, M. Tang, S. J. Dillon, J. Luo, G. S. Rohrer, and M. P. Harmer, Acta Materialia **62**, 1 (2014).
[59] P. R. Cantwell, T. Frolov, T. J. Rupert, A. R. Krause, C. J. Marvel, G. S. Rohrer, J. M. Rickman, and M. P. Harmer, Annual Review of Materials Research **50**, 465 (2020).
[60] S. Johansson and G. Wahnström, Acta Materialia **59**, 171 (2011).
[61] M. Menahem, Z. Dai, S. Aharon, R. Sharma, M. Asher, Y. Diskin-Posner, R. Korobko, A. M. Rappe, and O. Yaffe, ACS Nano **15**, 10153 (2021).
[62] S. Zuri, A. Shapiro, L. Kronik, and E. Lifshitz, The Journal of Physical Chemistry Letters **14**, 4901 (2023).
[63] G. C. Papavassiliou, G. A. Mousdis, C. P. Raptopoulou, and A. Terzis, Zeitschrift für Naturforschung B **54**, 1405 (1999).
[64] G. Kresse and J. Hafner, Physical Review B **47**, 558 (1993).
[65] G. Kresse and J. Furthmüller, Physical Review B **54**, 11169 (1996).
[66] G. Kresse and J. Furthmüller, Computational Materials Science **6**, 15 (1996).
[67] P. E. Blöchl, Physical Review B **50**, 17953 (1994).
[68] G. Kresse and D. Joubert, Physical Review B **59**, 1758 (1999).
[69] H. Peng, Z.-H. Yang, J. P. Perdew, and J. Sun, Physical Review X **6**, 041005 (2016).
[70] E. Fransson, J. Wiktor, and P. Erhart, The Journal of Physical Chemistry C **127**, 13773 (2023).
[71] Z. Fan, Z. Zeng, C. Zhang, Y. Wang, K. Song, H. Dong, Y. Chen, and T. Ala-Nissila, Physical Review B **104**, 104309 (2021).
[72] Z. Fan, Journal of Physics: Condensed Matter **34**, 125902 (2022).
[73] Z. Fan, Y. Wang, P. Ying, K. Song, J. Wang, Y. Wang, Z. Zeng, K. Xu, E. Lindgren, J. M. Rahm, A. J. Gabourie, J. Liu, H. Dong, J. Wu, Y. Chen, Z. Zhong, J. Sun, P. Erhart, Y. Su, and T. Ala-Nissila, The Journal of Chemical Physics **157**, 114801 (2022).
[74] Z. Fan, W. Chen, V. Vierimaa, and A. Harju, Computer Physics Communications **218**, 10 (2017).
[75] E. Fransson, P. Rosander, P. Erhart, and G. Wahnström, Chemistry of Materials **36**, 514 (2023).
[76] X. Liang, J. Klarbring, W. J. Baldwin, Z. Li, G. Csányi, and A. Walsh, The Journal of Physical Chemistry C **127**, 19141 (2023).

Supplemental Material:

Impact of Surface Adsorbates and Dimensionality in Templating of Halide Perovskites

Erik Fransson[1], Julia Wiktor[1], and Paul Erhart[1]

[1] *Department of Physics, Chalmers University of Technology, SE-41296, Gothenburg, Sweden*

May 9, 2024

Contents

1 NEP model

We construct a neuroevolution potential (NEP) model using the bootstrapping and active learning strategy outlined in Ref. 1 using the GPUMD software.[2–4] The resulting training and validation errors obtained by cross validation with 10 folds are shown in Fig. S1.

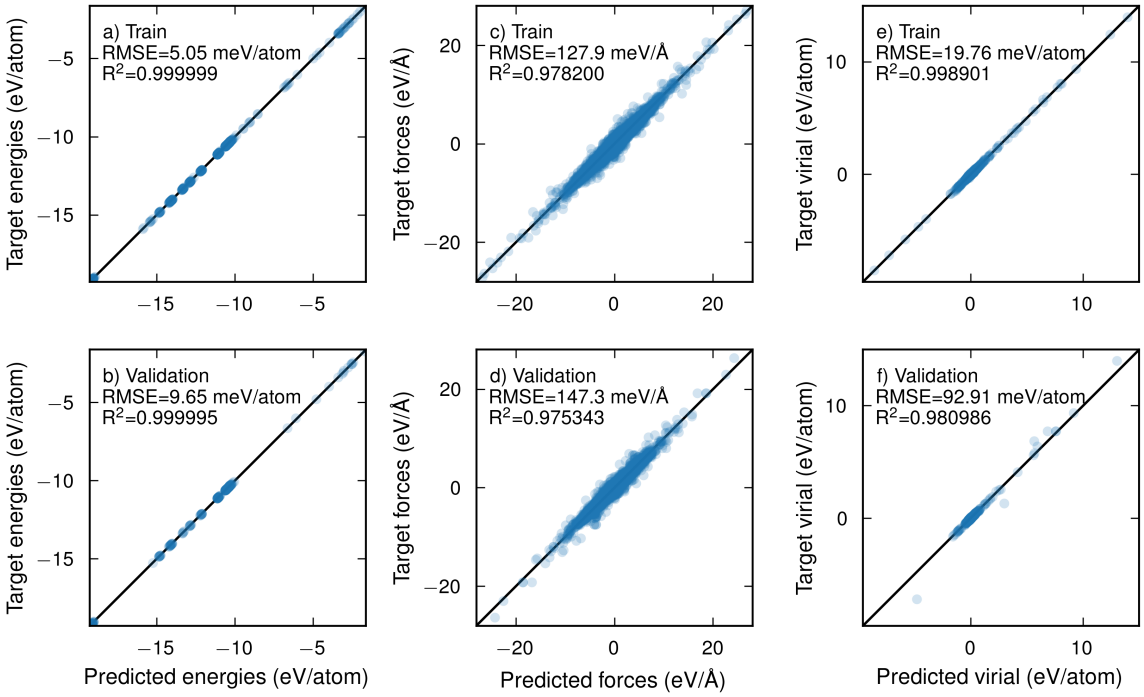

Figure S1: Parity plots for total energies, forces and virials for training and validation sets.

2 Additional analysis of cooling simulations

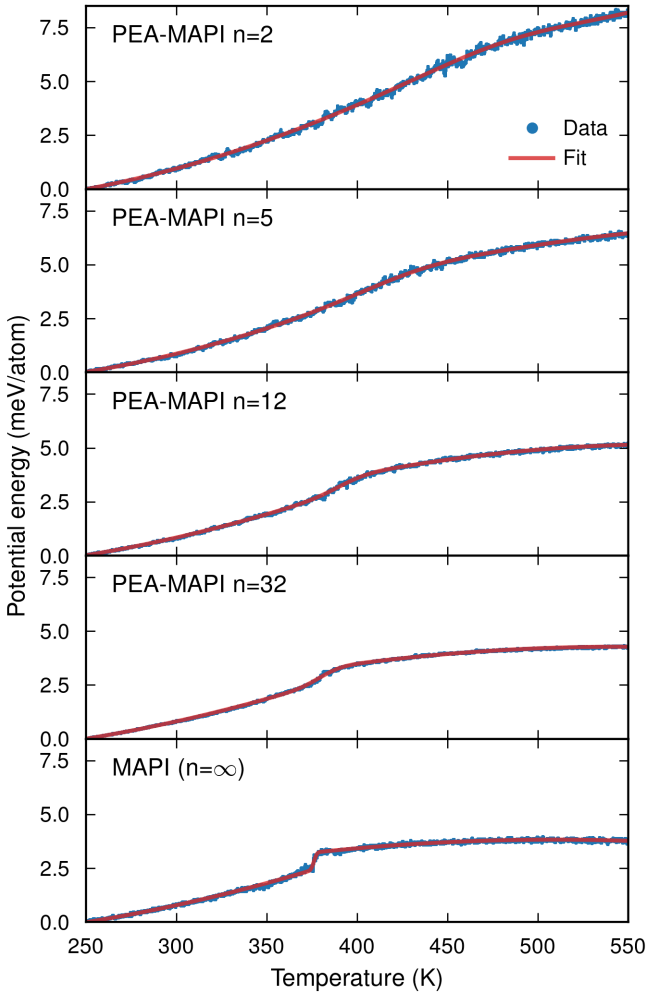

Figure S2: Potential energy data from cooling simulations averaged using a gliding window with a size corresponding to 0.4 K and fits to two polynomials splined together with an error function.

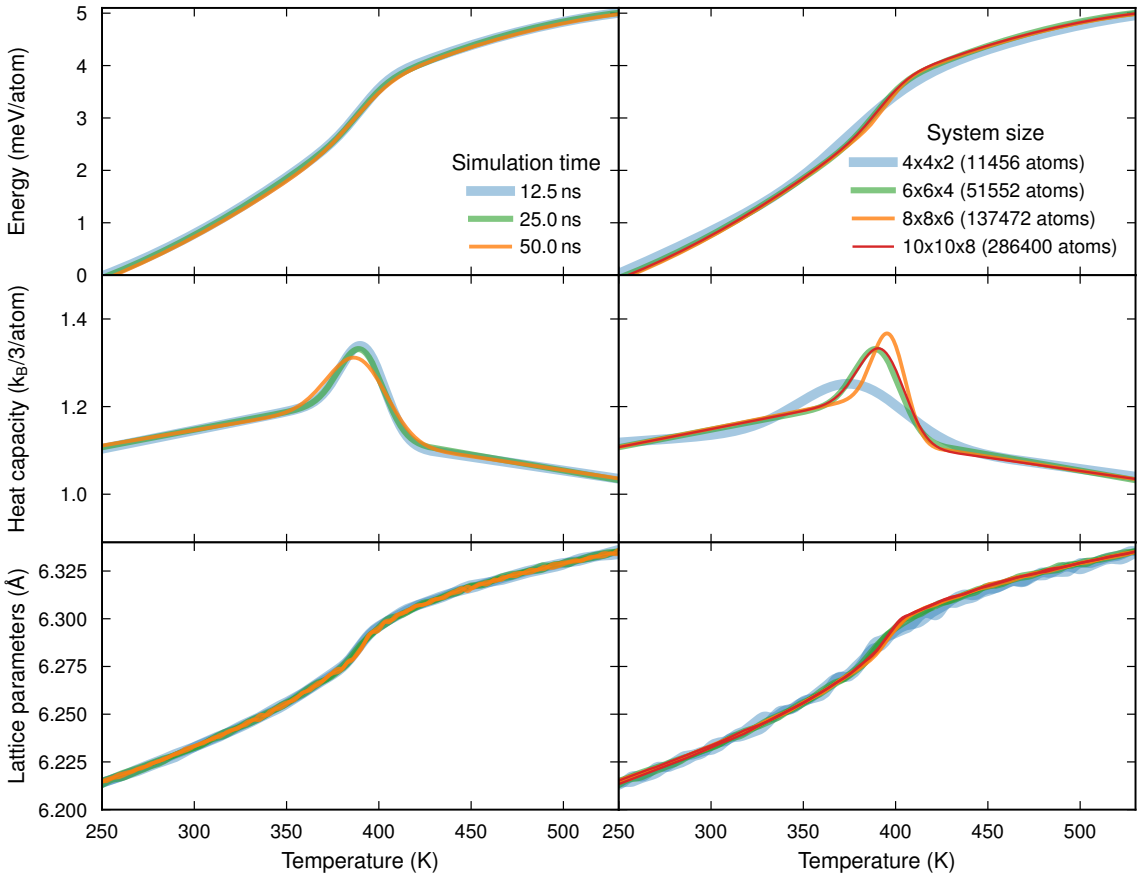

Figure S3: Convergence of potential energy, heat capacity and in-plane lattice-parameters with respect to simulation time (left) and system size (right) for PEA-$MAPbI_3$ $n = 12$. Unless specified the system size and simulation length are the same as used in the remainder of this paper, i.e., $6 \times 6 \times 4$ and 25 ns.

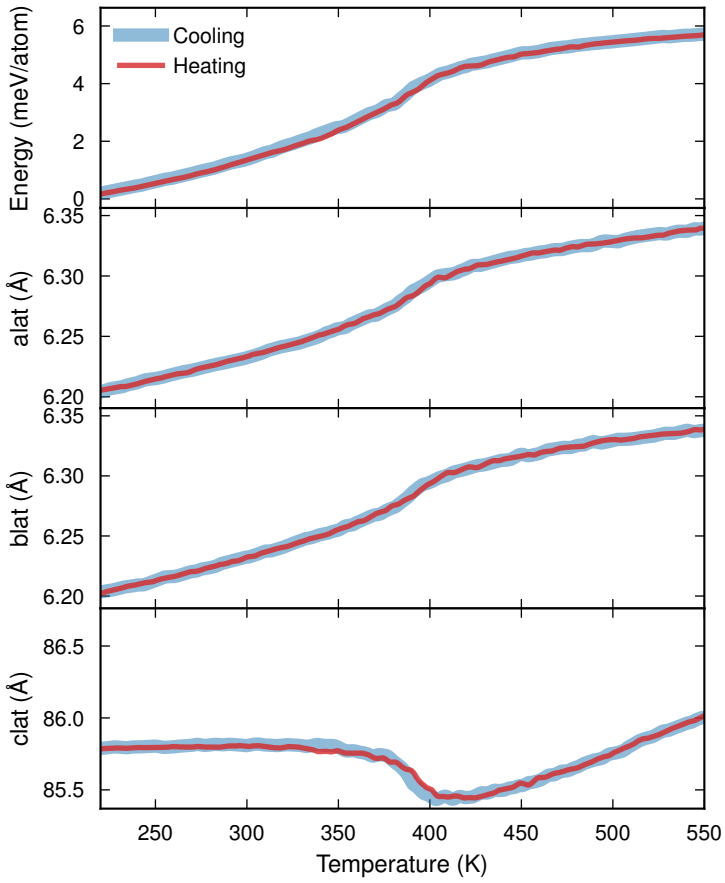

Figure S4: Thermodynamic properties from heating and cooling runs for PEA-MAPbI$_3$ with $n = 12$.

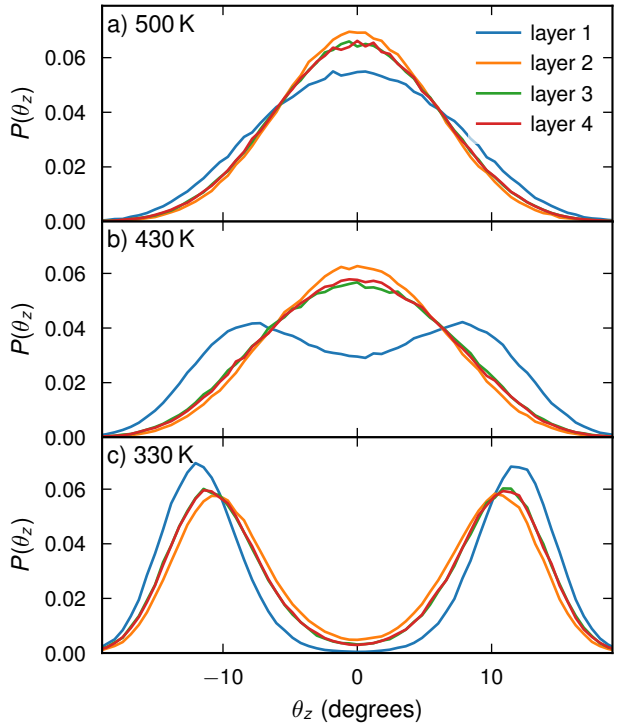

Figure S5: Probability distribution over the octahedral tilt angles, $P(\theta_z)$, for each symmetrically distinct layer in PEA-MAPbI$_3$ with $n = 8$ at (a) 500 K, (b) 430 K and (c) 330 K. Here, layer 1 refers to the perovskite layer closes to the organic linker molecule.

3 Transitions in additional systems

Here, we consider the cooling runs of phenylmethylammonium $C_6H_5(CH_2)NH_3$ (PMA)-$MAPbI_3$, butylammonium $CH_3(CH_2)_3NH_3$ (BA)-$MAPbI_3$ and the $MAPI_3$ surface {001} surface. We note that there is some uncertainty of about $\pm 10\,\mathrm{K}$ when determining the transition temperatures from the tilt angle analysis as done here due to the stochastic nature of the molecular dynamics (MD) simulations. For example, perovskite regions separated by the linker can undergo the transitions at slightly different points of time in the MD simulations, and the presence of anti-phase boundaries leads to small changes in the transition temperature.

One should also note that the NEP model overestimates the $MAPbI_3$ bulk transition temperature by about $40\,\mathrm{K}$ compared to experiment. We therefore emphasize that these results should be interpreted in a qualitative or semi-qualitative manner.

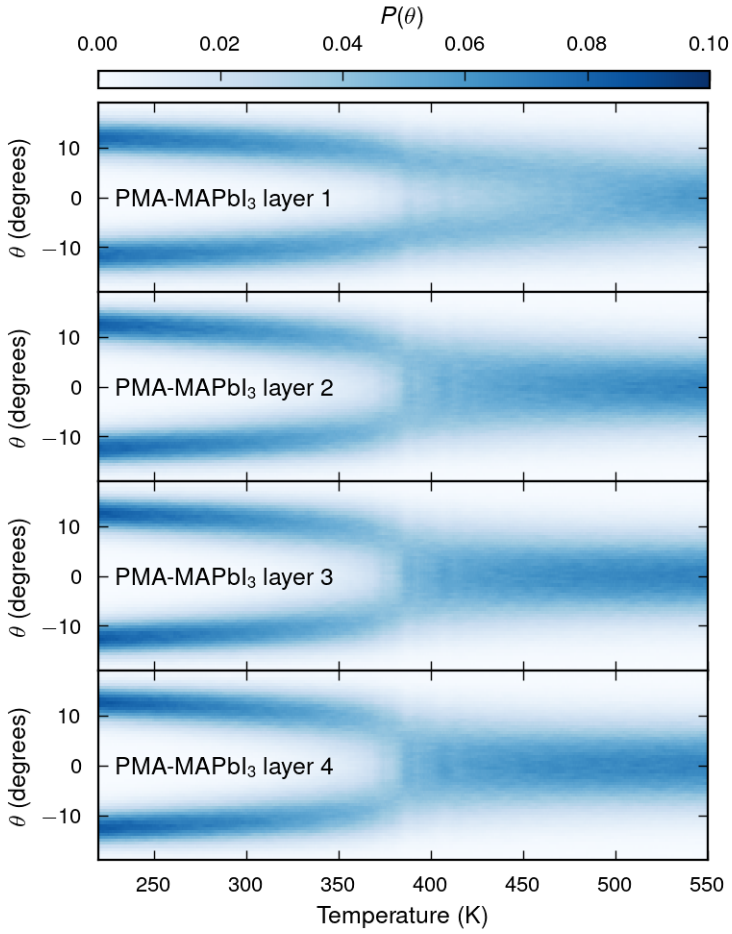

Figure S6: Probability distribution over the octahedral tilt angles, $P(\theta)$, as a function of temperature for PMA-$MAPbI_3$ with $n = 8$.

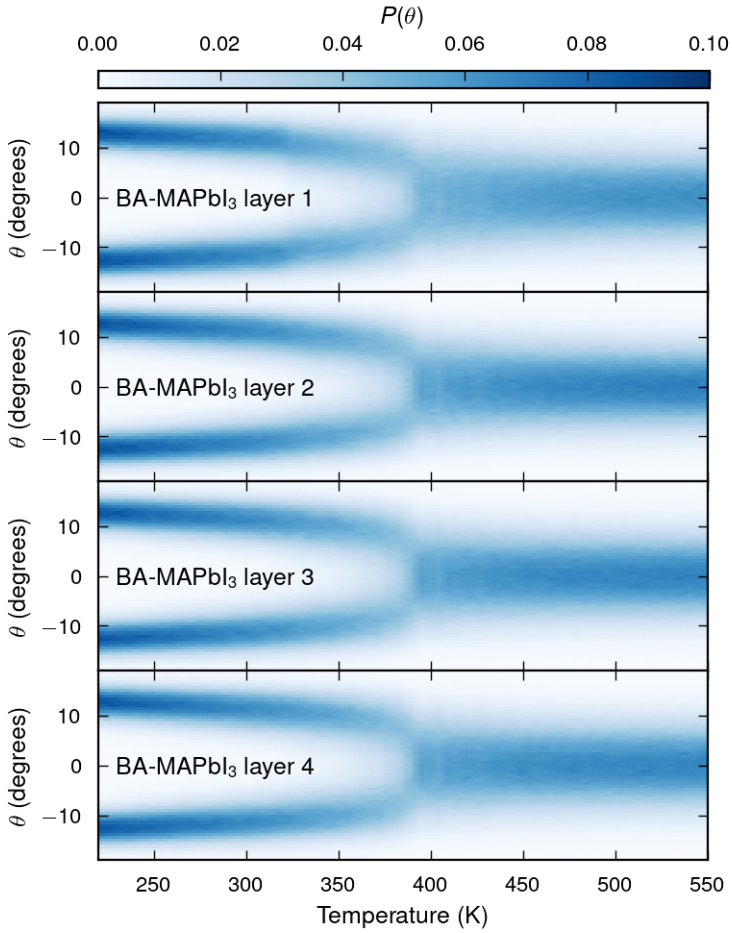

Figure S7: Probability distribution over the octahedra tilt angles, $P(\theta)$, as a function of temperature for BA-MAPbI$_3$ with $n = 8$.

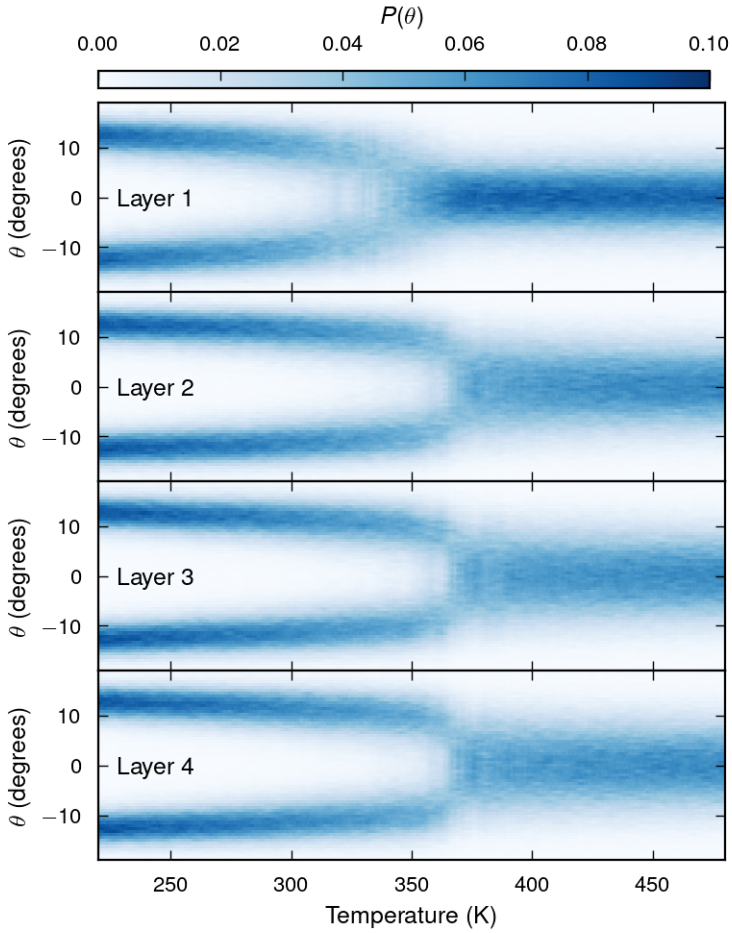

Figure S8: Probability distribution over the octahedral tilt angles, $P(\theta)$, as a function of temperature for a pure $MAPbI_3$ {001} surface with MAI_2 termination with a total of 16 perovskite unit cells in the z-direction. Here, the tilt angles are shown for the first four layers starting with the top-most surface layer.

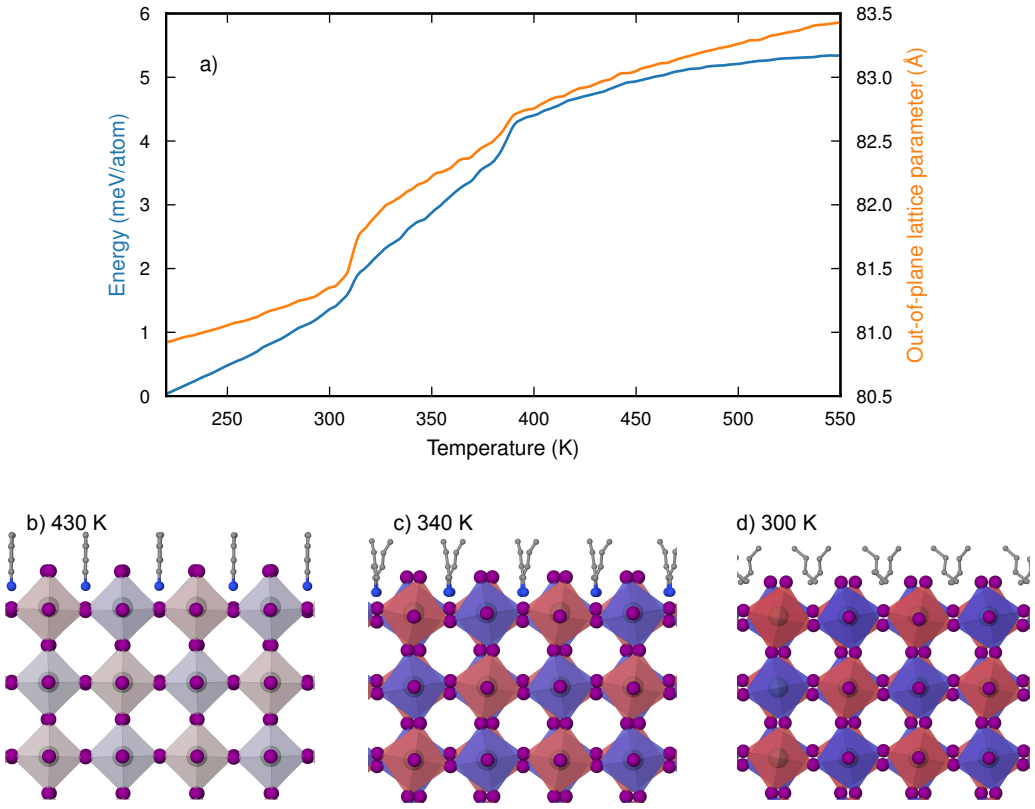

Figure S9: (a) Energy and out-of-plane lattice parameter for BA-$MAPbI_3$ with $n = 12$. At about 380 K one observes the transition between the untilted and the tilted structure, and around 300 K there is a transition related to freezing in the BA molecules in a "bent" configuration leading to a significant drop in the out-of-plane lattice parameter. (b–d) Average atomic configurations at (b) 430 K, (c) 340 K and (d) 300 K. Red and blue octahedra indicate negative and positive tilt angles (ranging from -20 to $20°$), respectively, whereas gray implies tilt angles close to zero.

Supplemental References

[1] Erik Fransson, Julia Wiktor, and Paul Erhart. Phase transitions in inorganic halide perovskites from machine-learned potentials. *The Journal of Physical Chemistry C*, 127(28):13773–13781, July 2023. doi: 10.1021/acs.jpcc.3c01542.

[2] Zheyong Fan, Zezhu Zeng, Cunzhi Zhang, Yanzhou Wang, Keke Song, Haikuan Dong, Yue Chen, and Tapio Ala-Nissila. Neuroevolution machine learning potentials: Combining high accuracy and low cost in atomistic simulations and application to heat transport. *Physical Review B*, 104:104309, Sep 2021. doi: 10.1103/PhysRevB.104.104309.

[3] Zheyong Fan. Improving the accuracy of the neuroevolution machine learning potential for multi-component systems. *Journal of Physics: Condensed Matter*, 34(12):125902, jan 2022. doi: 10.1088/1361-648x/ac462b.

[4] Zheyong Fan, Yanzhou Wang, Penghua Ying, Keke Song, Junjie Wang, Yong Wang, Zezhu Zeng, Ke Xu, Eric Lindgren, J. Magnus Rahm, Alexander J. Gabourie, Jiahui Liu, Haikuan Dong, Jianyang Wu, Yue Chen, Zheng Zhong, Jian Sun, Paul Erhart, Yanjing Su, and Tapio Ala-Nissila. GPUMD: A package for constructing accurate machine-learned potentials and performing highly efficient atomistic simulations. *The Journal of Chemical Physics*, 157(11):114801, September 2022. doi: 10.1063/5.0106617.